

ARTICLE

<https://doi.org/10.1038/s41467-019-12939-3>

OPEN

Structural water and disordered structure promote aqueous sodium-ion energy storage in sodium-birnessite

Xiaoqiang Shan ¹, Fenghua Guo¹, Daniel S. Charles¹, Zachary Lebens-Higgins ², Sara Abdel Razeq², Jinpeng Wu³, Wenqian Xu⁴, Wanli Yang ³, Katharine L. Page ⁵, Joerg C. Neufeind ⁵, Mikhail Feygenson ^{5,6}, Louis F.J. Piper ² & Xiaowei Teng ^{1*}

Birnessite is a low-cost and environmentally friendly layered material for aqueous electrochemical energy storage; however, its storage capacity is poor due to its narrow potential window in aqueous electrolyte and low redox activity. Herein we report a sodium rich disordered birnessite ($\text{Na}_{0.27}\text{MnO}_2$) for aqueous sodium-ion electrochemical storage with a much-enhanced capacity and cycling life (83 mAh g^{-1} after 5000 cycles in full-cell). Neutron total scattering and in situ X-ray diffraction measurements show that both structural water and the Na-rich disordered structure contribute to the improved electrochemical performance of current cathode material. Particularly, the co-deintercalation of the hydrated water and sodium-ion during the high potential charging process results in the shrinkage of interlayer distance and thus stabilizes the layered structure. Our results provide a genuine insight into how structural disordering and structural water improve sodium-ion storage in a layered electrode and open up an exciting direction for improving aqueous batteries.

¹Department of Chemical Engineering, University of New Hampshire, Durham, NH 03824, USA. ²Department of Physics, Applied Physics and Astronomy, Binghamton University, Binghamton, NY 13902, USA. ³Advanced Light Source, Lawrence Berkeley National Laboratory, Berkeley, CA 94720, USA.

⁴Advanced Photon Source, Argonne National Laboratory, Argonne, IL 60439, USA. ⁵Chemical and Engineering Materials Division, Spallation Neutron Source, Oak Ridge National Laboratory, Oak Ridge, TN 37831, USA. ⁶Juelich Centre for Neutron Science, Forschungszentrum Juelich GmbH, 52425 Juelich, Germany. *email: xw.teng@unh.edu

Electrochemical energy storage (EES) using earth-abundant materials has become attractive for storing electric energy generated by solar and wind¹. Aqueous EES using sodium (Na)-ion as charge carrier is promising alternative to non-aqueous lithium (Li)-ion batteries (LIBs) owing to low cost, high safety and the availability of Na sources in terrestrial reserves². However, Na-ion storage is challenging for its large radius. Consequently, LIB host materials (especially cathode) that typically have a close-packed array of oxide ions are able to reversibly accommodate Na-ions. Two design principles are used to tackle the issue. One is to replace oxygen anions (O^{2-}) with anions having weaker bonding with metal cations so that cations are sufficiently mobile in the electrode. Recent studies show promise of hexacyano ion ($C\equiv N$)₆⁶⁻ based electrode materials for Na- and K-ion storage due to the weakened bonding between cyanide ($C\equiv N$)⁻ and cations. Cui and co-workers have demonstrated that potassium copper hexacyanoferrate and its analogues can function as stable electrode materials for aqueous K- and Na-ion storage^{3–5}. Sodium-manganese hexacyanoferrate reported by Goodenough's group showed good energy performance and cycling life in a non-aqueous electrolyte^{6–8}. Another approach is to use a large interstitial host framework, especially layered structure. Layered materials with planar or zigzag layers show different polymorphs (P2, P3 or O2, O3 phase) with respect to the sites of intercalated Na-ion by simply altering the stacking of transition-metal-oxygen octahedra^{9–11}. Pioneer works on studying Na-ion intercalation in layered Na_xMnO_2 were reported by Hagemuller in the 1980s^{12,13}. However, the mechanistic understanding of Na-ion storage inside various host materials is still not settled. Size difference between Na-ion and Li-ion gives rise to different intercalation chemistries¹⁴, so that the understanding obtained from Li-ion storage may not be directly applied to the Na-ion electrodes^{15–18}. In addition, layered Na_xMnO_2 especially P-type materials where Na-ions occupy trigonal prismatic site suffer from P2-O2 phase transition during charging with a large lattice collapse and up to 23% of volume shrinkage, resulting in an increased Na-ion diffusion barrier and rapid capacity decay^{19,20}.

Birnessite (δ - MnO_2) is a layered structure comprised of two-dimensional sheets of edge-sharing MnO_6 octahedra with intercalated cations and/or water in the interlayer^{21–25}. Although birnessite has a large interlayer distance ($\sim 7 \text{ \AA}$), its storage capacities for Na-ion were low due to the limited thermodynamically stable potential window ($\sim 1.23 \text{ V}$) of an aqueous electrolyte and ineffective redox process^{26–28}. Recent studies showed that a concentrated Li-bis(trifluoromethane sulfonyl) imide salt in water electrolyte helped the formation of an

electrode-electrolyte interphase on a Mo_6S_8 anode that prevented the direct contact between anode and water, thus achieved potential window of 3.0 V for aqueous EES²⁹. A similar wide potential window was reported for aqueous electrolyte using hydrate-melt of Li salts^{30,31}. However, little work has been reported to date on how to widen the potential window of birnessite electrode materials in aqueous electrolytes.

Here we present an effective strategy to significantly improve the discharge capacity and cycle life of birnessite (full-cell capacity of 83 mAh g^{-1} at 1 A g^{-1} after 5000 cycles) through increasing the stable potential window and promoting redox charge transfer process towards aqueous Na-ion storage. Our results demonstrate that Na-rich and disordered birnessite structure can afford a stable potential window of 2.5 V in an aqueous electrolyte with high overpotential towards the gas evolution reactions. Moreover, co-deintercalation of water molecules along with Na-ion at the high potential charging, evidenced by in situ XRD, can stabilize the layered structure from over-expansion of the interlayer distance.

Results

Structural characterizations and formation mechanism. Different from wet chemistry synthesis of birnessite^{24,25,27,32}, disordered and Na-rich birnessite were prepared at 270 °C in air via a solid-state reaction between NaOH and Mn_3O_4 nanoparticles (Mn_3O_4 particles were synthesized using a method reported previously³³). By altering the molar ratios between NaOH and Mn_3O_4 , sodium-intercalated manganese oxides ($Na_\delta MnO_x$; δ : 0.10, 0.17, and 0.27) were prepared, verified by Inductively Coupled Plasma Mass Spectrometry (ICP-MS) (Supplementary Table 1). The Na/Mn ratio remained around 0.27 even when a higher NaOH/ Mn_3O_4 ratio of 4 was used (Supplementary Figure 1). The Na/Mn ratio of 0.27 is higher than those of birnessite materials reported (Supplementary Table 2)^{21–25}. Figure 1a and Supplementary Fig. 2 show that as Na concentrations increased from 0.10 to 0.27, the morphologies of resulting Na–Mn–O materials evolved from a mixture of faceted particles and planar structures to a complete planar structure. The atomic ordering of the resulting Na–Mn–O materials was analyzed using neutron total scattering and the atomic pair distribution function (PDF) (Fig. 1b), from which both the Bragg and diffuse scattering were analyzed to provide local structural details such as defects, mismatch or disorder at the atomic level. The structural parameters of various $Na_\delta MnO_x$ materials obtained from refinement are summarized in Supplementary Fig. 3 and Supplementary Table 3–6. The neutron PDF showed that the coherent length of

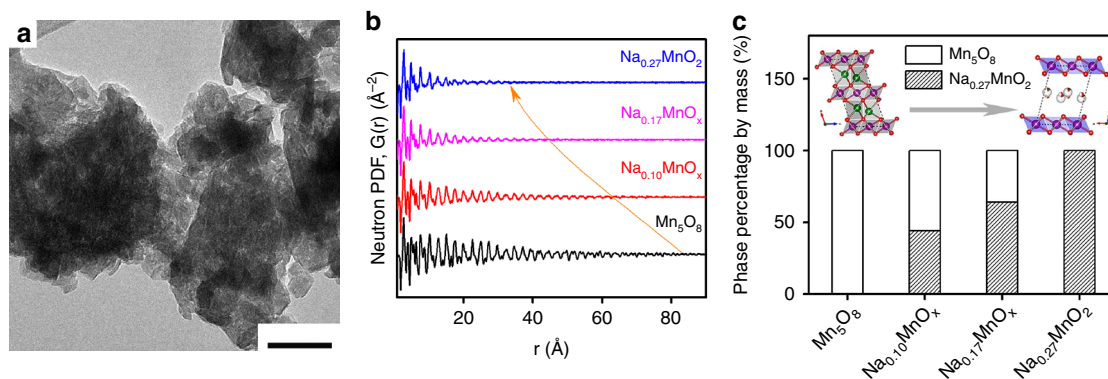


Fig. 1 TEM and neutron PDF analysis of sodium-manganese oxides. **a** TEM image of $Na_{0.27}MnO_2$ materials; scale bar, 50 nm; **b** Experimental neutron PDFs of $Na_\delta MnO_x$ materials, where coherent lengths, defined as the longest interatomic distance of the material, decreased as the Na concentration increased; **c** Phase percentage of $Na_{0.27}MnO_2$ in $Na_\delta MnO_x$ materials obtained from neutron PDF analysis

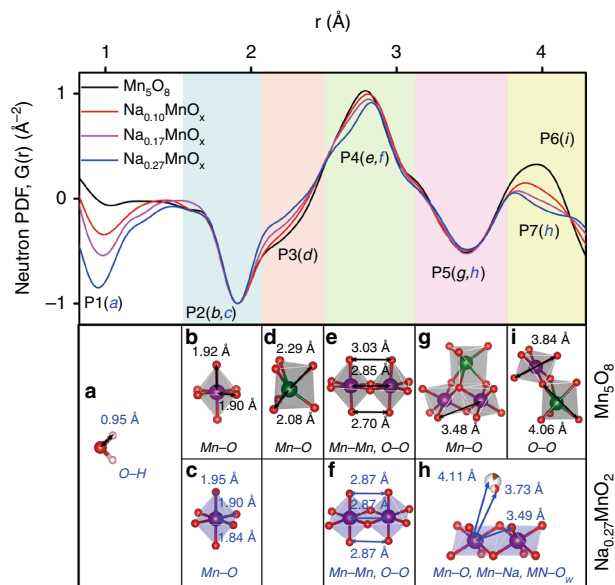


Fig. 2 Neutron PDFs of various $\text{Na}_\delta\text{MnO}_x$ materials. The atom pair associated with each peak (P1 to P7) can be attributed to **a** water, **b, d, e, g, i** Mn_5O_8 polyhedra in black and **c, f, h** MnO_2 polyhedra in blue

$\text{Na}_\delta\text{MnO}_x$ materials (a distance at which the peaks of atomic pairs vanished) decreased from >50 Å to ~ 30 Å as δ increases, indicating more confined crystalline order. Namely, $\text{Na}_\delta\text{MnO}_x$ materials cannot sustain long-range crystallinity and became more disordered when more Na-ions are incorporated into the structure. Figure 1c shows that as Na concentration (δ) increased, $\text{Na}_\delta\text{MnO}_x$ materials showed pure phase Mn_5O_8 ($\delta = 0$), mixture of Mn_5O_8 and layered MnO_2 ($\delta = 0.10$ and 0.17). When δ reached 0.27 , a pure triclinic birnessite structure formed with an interplanar distance of 7.19 Å. The chemical formula was determined as $\text{Na}_{0.27}\text{MnO}_2 \cdot 0.63\text{H}_2\text{O}$, where the Na^+ and structural water (determined from thermal gravimetric analysis shown in Supplementary Fig. 5) occupied the interlayers.

Neutron PDF studied the evolution of local structure during the transition from Mn_3O_4 to Mn_5O_8 , and finally to MnO_2 birnessite (Fig. 2). The PDF data were normalized by the intensity of the peak at 1.9 Å to see the comparative changes of the structural details as δ increased, and the original coherent scattering and structure factor data can be found in Supplementary Fig. 6. The peaks of PDF can be indexed as O–H pair (0.95 Å, P1) from water (a), one Mn–O pair (1.9 Å, P2) from the $[\text{MnO}_6]$ octahedral unit and another Mn–O pair (2.2 Å, P3) from Mn atoms in prismatic sites, Mn–Mn or O–O pair (2.8 Å, P4), and Mn–O pair (3.5 Å, P5) from the nearest neighbors of $[\text{MnO}_6]$ octahedral units, respectively. The contribution of individual pairs such as Mn–O, Mn–Mn, O–O, and Mn–Na, to the overall PDF of the materials can be found in Supplementary Figure 7. Notably O–H pair (P1) and Mn–O pairs (P2, P3, P5, and P7) showed negative peaks due to negative coherent neutron scattering lengths of H and Mn atoms (-3.74 and -3.73 femtometer, respectively). The Mn–O pair (1.9 Å, P2) is attributed to Mn–O octahedral coordination in both Mn_5O_8 (b) and layered $\text{Na}_{0.27}\text{MnO}_2$ (c) structures. The Mn–O pair (2.2 Å, P3) is attributed to Mn(II)–O from Mn_5O_8 phase (d), which decreased relatively to Mn(IV)–O pair at P2 as δ increased, congruent with the decreasing phase fractions of Mn_5O_8 . The positive peaks at 2.8 Å (P4) are attributed to Mn–Mn or O–O bonding from adjacent $[\text{MnO}_6]$ octahedral units in Mn_5O_8 (e) and $\text{Na}_{0.27}\text{MnO}_2$ (f) relative to the Mn(IV)–O pair, which did not change significantly as δ increased. A similar trend can be found

in the Mn–O pair at 3.5 Å (P5) from adjacent $[\text{MnO}_6]$ in Mn_5O_8 (g) and $\text{Na}_{0.27}\text{MnO}_2$ phases (h). The peaks at ~ 4.0 Å (P6 and P7) showed a rather interesting transition from positive to negative direction as δ increased. The positive peak at 3.96 Å (P6) is related to O–O pairs (i) in Mn_5O_8 either within the same $[\text{Mn}(\text{IV})\text{O}_6]$ octahedral unit or $[\text{Mn}(\text{II})\text{–O}]$ units where Mn^{2+} is located in the trigonal prismatic site. In contrast, the negative peak at 4.0 Å (P7) is attributed to Mn–Na pair at 4.11 Å (h) from the interaction between Na-ions in interlayers and Mn^{4+} from $[\text{MnO}_6]$ octahedra or Mn–O_w pair (O_w from structural water in the interlayer) at 3.73 Å (h) from the interaction between H_2O in interlayers and Mn^{4+} , both from $\text{Na}_{0.27}\text{MnO}_2$ layered phase. The interplay between negative peaks of Mn–Na and Mn–O_w in $\text{Na}_{0.27}\text{MnO}_2$ and the positive peak of O–O in Mn_5O_8 at around 4.0 Å explains the overall peak change from positive to negative directions when δ increased. This suggests that phase transition from Mn_5O_8 to $\text{Na}_{0.27}\text{MnO}_2$ birnessite was driven by Na-ion insertion during solid-state annealing.

From neutron PDF and in situ XRD during the thermal treatment (Supplementary Fig. 8), a formation mechanism of $\text{Na}_{0.27}\text{MnO}_2$ birnessite is proposed in Fig. 3. Mn_3O_4 nanoparticles were first converted into Mn_5O_8 materials through oxidation of $[\text{Mn}(\text{III})\text{O}_6]$ octahedra of Mn_3O_4 into $[\text{Mn}(\text{IV})\text{O}_6]$ units, followed by Na-ion driven conversion from Mn_5O_8 to $\text{Na}_{0.27}\text{MnO}_2$ birnessite during the thermal annealing in air. Mn_5O_8 and $\text{Na}_{0.27}\text{MnO}_2$ share similar structural characteristics: Mn_5O_8 has a layered structure and consists of sheets of $[\text{Mn}_3^+\text{O}_8]^{4-}$ in the *bc* plane. The $[\text{Mn}_3^+\text{O}_8]^{4-}$ sheets resemble the structure of $\text{Na}_{0.27}\text{MnO}_2$ birnessite comprised of infinite $[\text{MnO}_6]$ octahedral layers with intercalated Na cations in between. The transition from Mn_5O_8 to $\text{Na}_{0.27}\text{MnO}_2$ birnessite is an equivalent process to the ion-exchange of Mn^{2+} ions in the $\text{Mn}_2^+\text{Mn}_3^+\text{O}_8$ with Na^+ ions in the solid state. Our result suggests that Mn^{2+} ions with trigonal prismatic coordination located in interlayers of Mn_5O_8 have a higher mobility than octahedrally coordinated Mn^{4+} ions. Therefore, insertion of Na-ions into the Mn^{2+} site was kinetically favored, accompanied by the oxidation of Mn^{2+} ions into Mn^{4+} during the migration of Mn^{2+} to the $[\text{Mn}^{4+}_3\text{O}_8]^{4-}$ layers, and drove the formation of $\text{Na}_{0.27}\text{MnO}_2$. XRD showed that anhydrous $\text{Na}_{0.27}\text{MnO}_2$ has an interlayer distance of 5.6 Å (Supplementary Fig. 9), similar to that of Mn_5O_8 (5.2 Å). Upon water intercalation, $\text{Na}_{0.27}\text{MnO}_2 \cdot 0.63\text{H}_2\text{O}$ showed an increased interlayer distance of 7.19 Å³⁴. Na-ion driven conversion from Mn_5O_8 to $\text{Na}_{0.27}\text{MnO}_2$ reported here contrasts the formation of Li– MnO_2 via the ion-exchange between $\text{Ca}_2\text{Mn}_3\text{O}_8$ ($\text{Ca}^{2+}_2\text{Mn}^{4+}_3\text{O}_8$), isomorphic structure of Mn_5O_8 ($\text{Mn}^{2+}_2\text{Mn}^{4+}_3\text{O}_8$), and molten lithium nitrate³⁵. In the formation of Li– MnO_2 , Li-ions occupied all the available octahedral sites between the $[\text{Mn}_3^+\text{O}_8]^{4-}$ layers rather than the trigonal prismatic sites occupied by Ca^{2+} in the parent $\text{Ca}_2\text{Mn}_3\text{O}_8$ compound due to much smaller size of Li^+ compared with Ca^{2+} , resulting in the complete conversion to layered LiMnO_2 with $R\bar{3}m$ or $O3$ symmetry.

Electrochemical properties. Electrochemical performance of various $\text{Na}_\delta\text{MnO}_x$ materials was tested in a 0.1 M Na_2SO_4 electrolyte in a three-electrode half-cell using cyclic voltammetry (CV) between -1.25 V and 1.25 V (vs Ag/AgCl) (Supplementary Fig. 10). Figure 4a shows the CVs of disordered Na-rich $\text{Na}_{0.27}\text{MnO}_2$, where distinct redox peaks can be observed at all the tested scan rates. Figure 4a shows that when scan rate increased, $\text{Na}_{0.27}\text{MnO}_2$ shows small peak shifts in the anodic process (0.12 V) and the cathodic process (0.14 V), compared with the other $\text{Na}_\delta\text{MnO}_x$ materials (Supplementary Fig. 11), indicating Na-ion transport in $\text{Na}_{0.27}\text{MnO}_2$ required a lower

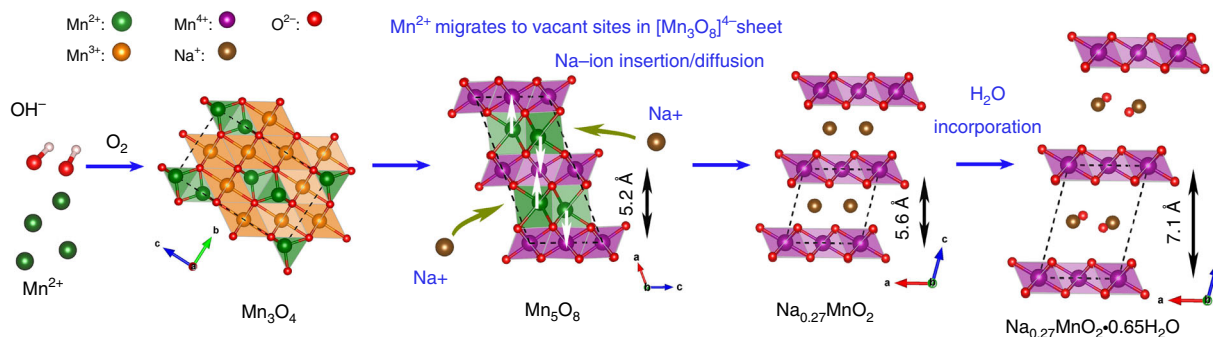


Fig. 3 The schematic of the formation mechanism. The proposed Na-ion driven intercalation in the formation of $\text{Na}_{0.27}\text{MnO}_2 \cdot 0.65\text{H}_2\text{O}$ materials in solid-state (Mn^{2+} : green; Mn^{3+} : orange; Mn^{4+} : purple; Na^+ : brown; O: red)

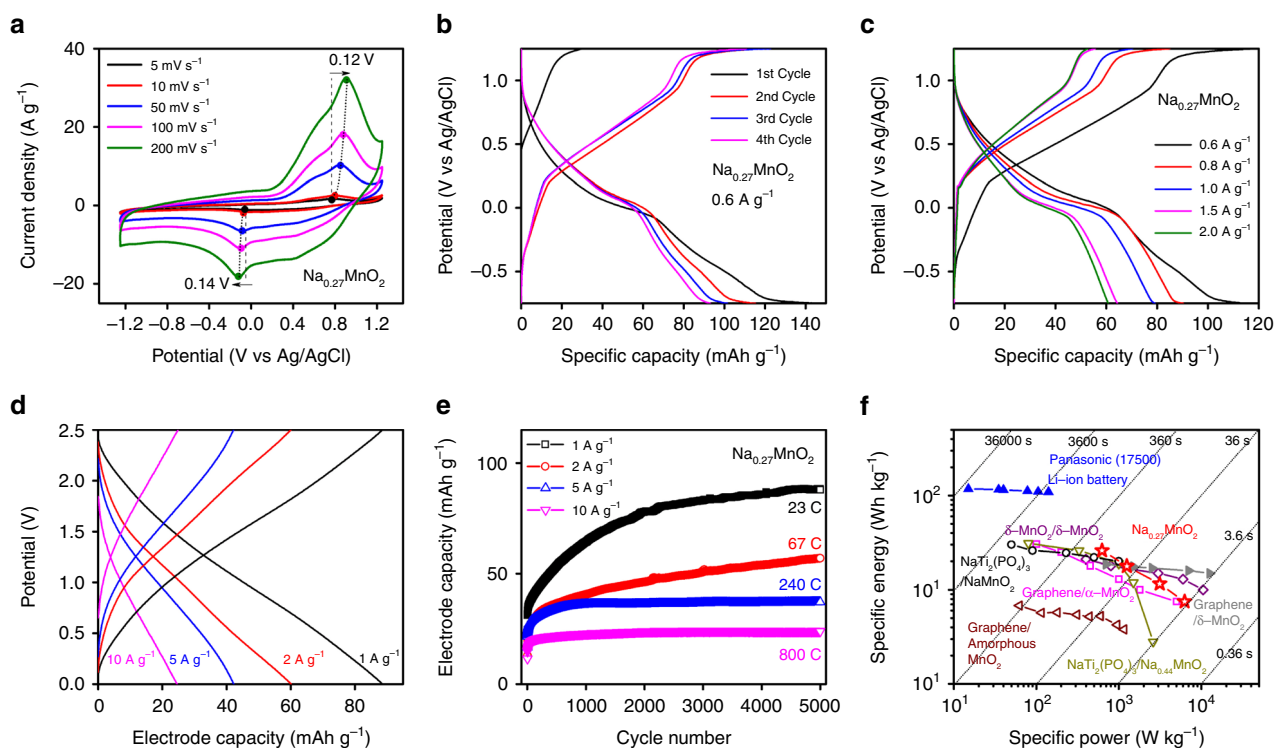


Fig. 4 Electrochemical measurements of $\text{Na}_{0.27}\text{MnO}_2$ in half-cells and full-cells. Electrochemical half-cell measurements with **a** CV scans of $\text{Na}_{0.27}\text{MnO}_2$ material between -1.25 V and 1.25 V (vs Ag/AgCl) at various scan rates in 0.1 M Na_2SO_4 electrolyte; **b** CP tests of $\text{Na}_{0.27}\text{MnO}_2$ material between -0.75 V and 1.25 V (vs Ag/AgCl) at a current density of 0.6 A g^{-1} in 0.1 M Na_2SO_4 electrolyte with the initial four charge and discharge cycles **c** CP tests of $\text{Na}_{0.27}\text{MnO}_2$ material between -0.75 V to 1.25 V (vs Ag/AgCl) at current densities ranging from 0.6 to 2.0 A g^{-1} in 0.1 M Na_2SO_4 electrolyte (2nd cycle data). Symmetric full-cell measurements with **d** charge and discharge electrode capacities of $\text{Na}_{0.27}\text{MnO}_2$ material at the various current densities of 1 A g^{-1} , 2 A g^{-1} , 5 A g^{-1} , and 10 A g^{-1} (after 5000 galvanostatic charge and discharge process unless specified otherwise); **e** electrode capacities of $\text{Na}_{0.27}\text{MnO}_2$ as a function of cycle number up to 5000 at the current densities from 1 A g^{-1} to 10 A g^{-1} ; **f** Ragone plot with gravimetric specific energy and power of the symmetric $\text{Na}_{0.27}\text{MnO}_2$ full-cell after 5000 galvanostatic cycles. The aqueous (empty symbols) and non-aqueous (solid symbols) devices are reported, and the gravimetric specific energy and power are calculated by the mass of electrode materials except the Panasonic (17500) Li-ion batteries

overpotential at higher charging rates. Further quantitative evaluation of Na-ion transport in all $\text{Na}_\delta\text{MnO}_x$ materials was obtained using a current-pulse relaxation method¹³, where the $\text{Na}_{0.27}\text{MnO}_2$ material showed a highest diffusion coefficient of 38.7 (relative to Mn_5O_8) than the other $\text{Na}_\delta\text{MnO}_x$ materials (Supplementary Figure 12). This result was congruent with CV data, where $\text{Na}_{0.27}\text{MnO}_2$ had the lowest energy barrier for Na-ion intercalation since it had a more dominant phase of layered birnessite.

Figure 4b shows the galvanostatic chronopotentiometry (CP) tests of $\text{Na}_{0.27}\text{MnO}_2$ materials in half-cell at 0.6 A g^{-1} under the potential window between -0.75 V and 1.25 V (vs Ag/AgCl),

demonstrating a high discharge capacity of 138 mAh g^{-1} (1st cycle) and a capacity of 94 mAh g^{-1} after 4th cycle. A highest discharge capacity of 144 mAh g^{-1} was observed for Na-ion storage at a current density of 0.3 A g^{-1} (Supplementary Fig. 13), although additional capacity could be attributed to the hydrogen evolution reaction (HER). It is suggested that discharge capacity of 144 mAh g^{-1} could be the highest capacity of $\text{Na}_{0.27}\text{MnO}_2$ materials measured at three-electrode half-cell conditions, corresponding to 0.47 Na-ion transfer per Mn atom. As $\text{Na}_{0.27}\text{MnO}_2$ electrode materials was initially charged to 1.25 V from open circuit voltage of ~ 0.5 V with the 1st cycle charge capacity of 71 mAh g^{-1} , indicating a roughly 0.23 Na-ion removal. In the

following 1st cycle discharge process, the MnO₂ birnessite electrode displayed a discharge capacity about 144 mAh g⁻¹, pointing to 0.47 Na-ion insertion. Figure 4c shows CPs of Na_{0.27}MnO₂ in the three-electrode half-cell at current densities from 0.6 A g⁻¹ to 2 A g⁻¹. As current densities increased, discharged capacities decreased from 115 to 61 mAh g⁻¹. Moreover, Supplementary Figure 14 shows that the charge and discharge potential differences at the midpoint of the capacity increased from 0.65 V to 0.75 V as current densities increased, suggesting an increasing polarization for Na-ion transport, comparable to the values reported in Zn-MnO₂^{36–38}, Na-MnO₂³⁹, and Li₂Mn_{2/3}Nb_{1/3}O₂F system⁴⁰, reflecting the intrinsic redox barrier for the MnO₂ based electrode systems.

Supplementary Figure 15 shows X-ray photoelectron spectroscopy (XPS) spectra of Na_{0.27}MnO₂. The pristine state Mn showed a dominant Mn⁴⁺ state with characteristic Mn 2p_{1/2} and Mn 2p_{3/2} features at 654.2 eV and 642.5 eV, and less distinct but discernable Mn³⁺ features at 642.2 eV and 653.3 eV, respectively (Supplementary Fig. 16). The ratio between Mn⁴⁺ and Mn³⁺ was calculated to be 0.72:0.28. Since the Mn³⁺ resulted from the intercalated Na-ion in interlayers of MnO₂, a Mn⁴⁺/Mn³⁺ ratio of 0.72:0.28 suggested a Na/Mn ratio of 0.28, nearly identical to the ICP-MS result (Na:Mn = 0.27). At charged state (1.25 V) Na_{0.27}MnO₂ showed a Mn⁴⁺/Mn³⁺ ratio of 0.97:0.03, and a Mn⁴⁺/Mn³⁺ ratio of 0.62:0.38 at discharged state (-1.25 V). Although the exact determination of Mn^{2+/3+/4+} ratio is challenging from the Mn 2p core region due to the multiplet structure and significant overlap between different oxidation states, XPS results confirmed that Na_{0.27}MnO₂ materials had a Mn⁴⁺/Mn³⁺ redox couple during insertion and extraction of Na-ions.

We also analyzed the current (*i*) at different scan rates (*v*) at a given potential, assuming that the total current (*i*) at a particular potential contains both capacitive current ($i_1 = k_1 v$) and diffusion-limited redox current ($i_2 = k_2 v^{1/2}$):⁴¹

$$i = i_1 + i_2 = k_1 v + k_2 v^{1/2} \text{ or } i/v^{1/2} = k_1 v^{1/2} + k_2$$

The values of *k*₁ and *k*₂ and the relative current response from *i*₁ and *i*₂ can be obtained. The CVs marked with capacitive and diffusion-limited redox contributions at scan rates ranging from 5 to 1000 mV s⁻¹ can be found and summarized in Supplementary Figs. 17 and 18.

Long-term performance of Na_{0.27}MnO₂ was tested in symmetric full-cells in a potential window of 2.5 V. Toray paper was used as the current collector without causing gas evolution reactions (Supplementary Fig. 19). Figure 4d and Supplementary Fig. 20 show that voltage-capacity profiles are nearly linear at all the tested current densities, pointing to a single-phase solid solution reaction. Accordingly, electrode capacities were calculated to be 83 mAh g⁻¹ to 24 mAh g⁻¹ at corresponding discharge times ranging from 160 s to 4.5 s. Moreover, Na_{0.27}MnO₂ exhibits an excellent cycle stability up to 5000 cycles without obvious capacity loss, as well as nearly 100% coulombic efficiency and high energy efficiency at various current densities (Fig. 4e). Figure 4f compares the energy and power performance of Na_{0.27}MnO₂ materials with several aqueous or non-aqueous EES devices, including Panasonic (17500) Li-ion battery⁴², α-MnO₂, δ-MnO₂ or amorphous birnessites^{32,43–45}, and tunnel-structured Na_{0.44}MnO₂ and O3 type Na_xMnO₂^{39,46}. Notably, energy and power densities of our reported system were obtained after 5000 galvanostatic cycles, higher than those found in commercial products and recent literature. Comparisons between current works with other Mn-based electrode materials in aqueous storage are summarized in Supplementary Table 7^{43,46–48}.

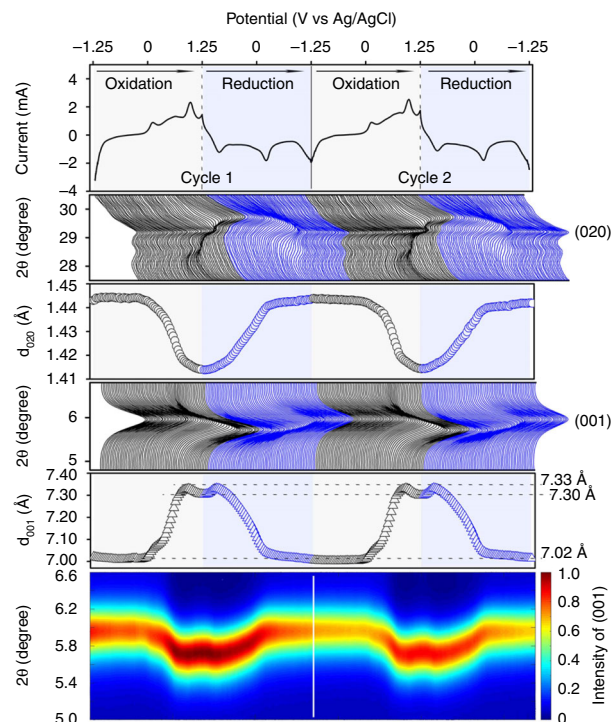


Fig. 5 In situ XRD characterization of Na_{0.27}MnO₂. Two CV scans were conducted between -1.25 V and 1.25 V at a scan rate of 0.75 mV s⁻¹, showing the changes of d-spacing for (001) basal diffraction plane and (020) Bragg diffraction plane and the contour plot peak variation of (001) plane during the charging (black) and discharging (blue) processes

Proton (H⁺) insertion has been reported in aqueous EES in mild acidic aqueous electrolytes^{36,37}. Current work used a neutral Na₂SO₄ electrolyte, thus the H⁺ concentration was very low and H⁺ intercalation may not contribute to overall storage capacity. In addition, Na_{0.27}MnO₂ materials showed continuously increasing capacities during the initial cycling especially at the low current densities. The electrochemical impedance spectroscopy measurements (Supplementary Fig. 21) demonstrate decreasing solution resistance during the initial electrochemical cycling, congruent with I-R drop in the discharge curves (Supplementary Fig. 22). It suggested that the increasing capacities in early cycles can be attributed to the slow building-up of a transport before the electrode reached its best electrochemical condition. Similar behaviours were also observed in Na-S, Na_{0.67}Ni_{1/6}Co_{1/6}Mn_{2/3}O₂, and LiFe_{0.9}P_{0.95}O₄^{49–51}.

Water co-deintercalation during high potential charging.

Supplementary Figure 23 shows in situ XRD measurements conducted along with the CV test at a scan rate of 0.75 mV s⁻¹, where diffraction peaks at the 2θ angles of ~5.8° and ~29° can be attributed to (001) basal diffraction peak and (020) Bragg peak, respectively. As shown in Fig. 5, when the potential increased from -1.25 V to 1.25 V (charging), the (001) peak shifted to a lower 2θ angle, corresponding to an increasing interlayer distance of (001) plane (*d*₀₀₁) because the electrostatic repulsion between the [MnO₆] layers leads to an increase of interlayer spacing upon the removal of Na-ions, whereas (020) Bragg peak shifted to a higher 2θ angle simultaneously with a decreasing *d*₀₂₀ due to the increased fraction of Mn⁴⁺ ions that have a smaller radius than Mn³⁺. During the reduction (from 1.25 V to -1.25 V), (001) and (020) peaks were restored to the original states. Nearly identical behaviors were also found in the second cycle. Na_{0.27}MnO₂ material showed a 4.4% change in the *d*₀₀₁ spacing of (from 7.33 Å

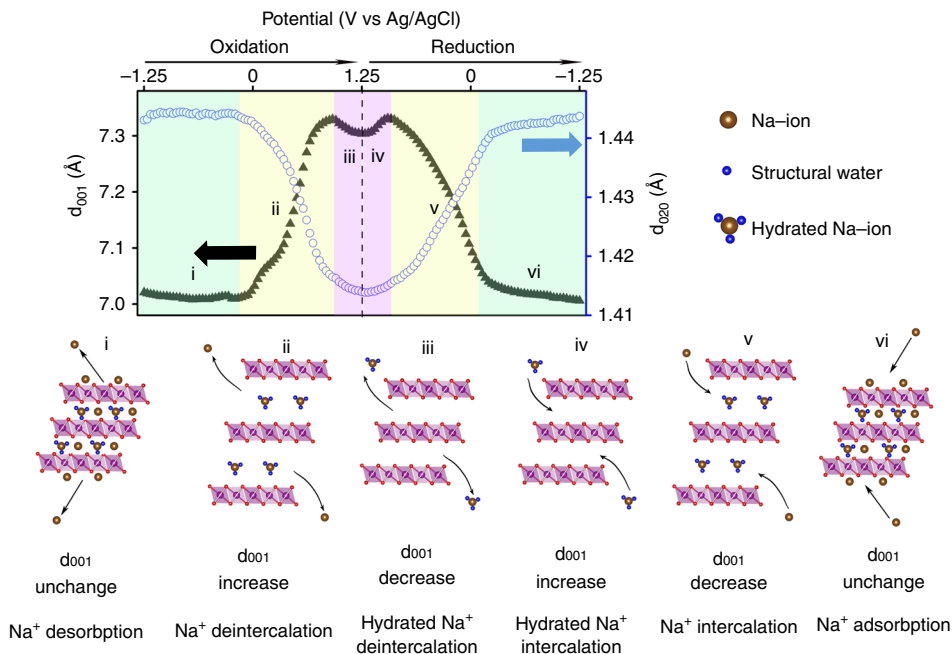


Fig. 6 Schematic of Na-ions and water motion during the redox processes. It shows co-deintercalation and co-intercalation of Na-ion and water molecules within the interlayer region of the $\text{Na}_{0.27}\text{MnO}_2$ during charging (oxidation) and discharging (reduction) processes

to 7.02 Å) between fully charged and discharged states, more significant than previously reported MnO_2 birnessite (1.7%) with a potential window of 1.2 V and a low capacity of 36 mAh g^{-1} ²⁷. The contour plot in Fig. 5 reflects peak shifts of the (001) basal diffraction peak of $\text{Na}_{0.27}\text{MnO}_2$ during charging and discharging process. The observed continuous and reversible peak shifting without a staged structural transformation indicates high structural stability of $\text{Na}_{0.27}\text{MnO}_2$ during the charging and discharging processes, which explains the good cycle life of $\text{Na}_{0.27}\text{MnO}_2$ materials.

In situ XRD also revealed water trafficking, for the first time, along with Na-ions insertion and extraction during the charging and discharging process. Figure 6 shows that when the potential increased from -1.250 V to -0.106 V, d_{001} and the corresponding electrochemical current remained relatively constant, suggesting a non-Faradaic capacitive charge storage process (e.g., desorption of Na-ions from electrode surface) without extracting Na-ions from interlayers. When the potential increased from -0.106 V to 0.914 V, d_{001} increased rapidly from 7.02 Å to 7.33 Å, indicating a large amount of Na-ions were extracted from the interlayers, concurrent with the increasing Faradaic current; as the potential continuously increased from 0.914 V to 1.25 V, d_{001} decreased from 7.33 Å to 7.30 Å. Interlayer collapse at higher potential is likely attributed to the removal of structural water along with Na-ion extraction, since a mere Na-ion removal alone would only cause an increase in d_{001} . Notably, such compression at high potential only happened in the interlayer distance (along *c*-direction) because d_{020} decreased continuously indicating continued oxidation of Mn^{3+} into Mn^{4+} when the potential increased from -0.106 V to 1.25 V. Although it is possible that when the potential increased from -0.106 V to 0.914 V the extracted Na-ions would also bring structural water out of the interlayer region, it was obvious that weakened electrostatic interaction caused by the Na-ion removal offsets the water removal effect if any, so that the overall interlayer distance still significantly increases. This means that extracted Na-ions at lower anodic potential range (from -0.106 V to 0.914 V) brought much less (or none) hydrated water molecules out of the interlayer

region compared with the ones extracted at higher anodic potential (from 0.914 V to 1.25 V). In other words, hydrated Na-ions required higher overpotential to be removed from interlayer region than less hydrated ones. It is possible that O ions (from water) in the solvation shell of the intercalated Na-ions could interact with Mn ions from Mn–O octahedral layer, especially when there are local defects (e.g., anion defect) and Mn cations are under-coordinated as previously reported interaction between V_2O_5 and structural water⁵². Such interaction could increase the energy barrier for Na-ion migration at charging process, and thus a higher overpotential will be needed to extract these hydrated Na-ion from host material. It is also possible that water molecules in the solvation shell of Na-ion could form hydrogen bonding in the interlayer region. This argument is also supported by a recent X-ray and neutron total scattering study of the birnessite materials, where hydrogen bonding among the interlayer water molecule and adjacent Mn–O layer oxygen ion was found to play an important role in maintaining the intermediate and long-range stacking of Mn–O octahedral layer⁵³. Therefore, hydrogen bonding between structural water could also stabilize the Na-ions inside the interlayer region, thus extraction these hydrated Na-ion out of interlayer region (charging) might become more difficult. Likewise, during the reduction process quite symmetric changes of d_{001} were observed: d_{001} slightly increased from 7.30 Å to 7.33 Å as the potential decreased from 1.25 V to 0.951 V, and then sharply decreased from 7.33 Å to 7.02 Å as the potential continued to decrease from 0.951 V to -0.682 V. This suggests that inserted Na-ions in the higher cathodic potential range (from 1.25 V to 0.951 V) brought more hydrated Na-ions into the interlayer region compared with ones inserted at lower anodic potentials (from 0.998 V to -0.682 V). Congruent with the observation of the water trafficking during the anodic scan, fully hydrated Na-ions preferred to be inserted into the interlayer region than less hydrated ones during the cathodic scan.

In conventional LIB layered oxide cathodes, a decrease in the *c*-lattice is widely observed at higher degrees of delithiation, even when there is no phase transformation⁵⁴. Recent work on a variety of $\text{LiNi}_{1-x-y}\text{Co}_x\text{Mn}_y\text{O}_2$ (NMC) compounds found the

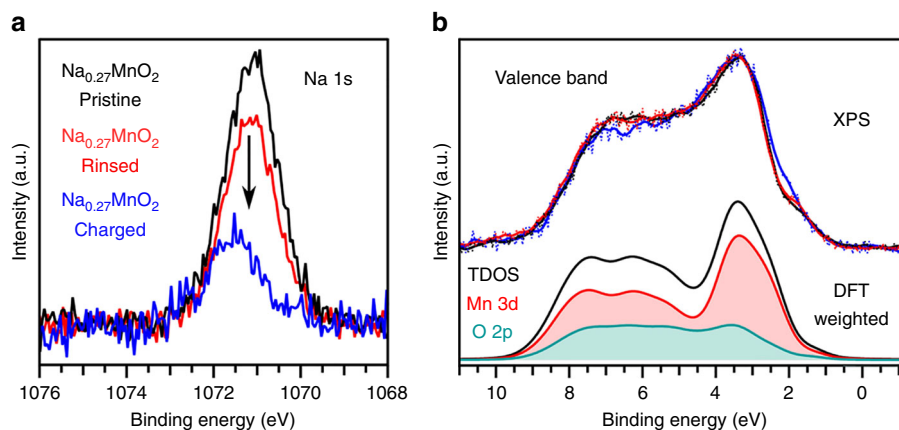


Fig. 7 XPS and DFT analysis of $\text{Na}_{0.27}\text{MnO}_2$. XPS measurements. **a** Na 1s region for pristine $\text{Na}_{0.27}\text{MnO}_2$ powder, $\text{Na}_{0.27}\text{MnO}_2$ powder rinsed in the Na_2SO_4 electrolyte, and **b** valence band of $\text{Na}_{0.27}\text{MnO}_2$ electrode charged to 1.25 V (vs Ag/AgCl). The valence band XPS spectra are compared with DFT calculations of the TDOS and the Mn 3d and O 2p PDOS for the $\text{Na}_{0.27}\text{MnO}_2$ system

onset of this decrease in the *c*-lattice when around 50–60% lithium has been removed from the structure with limited dependence on Ni, Co, or Mn content⁵⁵. In those LIB cathodes, strong nickel/cobalt-oxygen covalency is expected to facilitate charge transfer from the O 2p orbitals, decreasing the negative-charge on the oxygen⁵⁶. This effectively weakens electrostatic repulsions between neighboring oxygens across the Li-layer leading to a decrease in the interlayer spacing and thereby a decrease in the *c*-lattice. Upon relithiation, the *c*-lattice expands and can symmetrically match the collapse observed during delithiation^{55,57}. Density functional theory (DFT) calculations have shown this effect occurs for the LiMnO_2 system and may need to be considered for other Mn(IV)-systems⁵⁸.

We performed XPS measurements for pristine, rinsed, and charged $\text{Na}_{0.27}\text{MnO}_2$ in conjunction with DFT calculations, shown in Fig. 7. In this case, the charged $\text{Na}_{0.27}\text{MnO}_2$ is binder-free, which allowed for increased sensitivity to the $\text{Na}_{0.27}\text{MnO}_2$ compound (Supplementary Fig. 24). When charged to 1.25 V, there is a decrease in the intensity of the Na peak due to the removal of Na-ions from the interlayer (Fig. 7a). The corresponding valence band XPS measurements display only a slight change in the lineshape of the charged electrode compared to the pristine and rinsed samples likely related to the depopulation of states upon the removal of Na-ions. DFT calculations of the total density of states (TDOS) $\text{Na}_{0.27}\text{MnO}_2$ system weighted by the X-ray photoionization cross-section⁶ match well with the experimental spectra suggesting these calculations can be used to comment on Mn 3d–O 2p covalency (Fig. 7b). When looking at the weighted O 2p and Mn 3d partial density of states, we find O 2p states contribute at the top of the valence band (0 eV to 2 eV). At 1486 keV, the Mn 3d photoionization cross-section is over four times higher than the O 2p state so that in the unweighted DFT calculations the O 2p orbitals are the dominant contribution from 0 to 2 eV (Supplementary Fig. 25), i. e., there is discernable Mn–O covalency in the $\text{Na}_{0.27}\text{MnO}_2$ so that we may have to consider a decrease in the negative-charge on the oxygen with Na-removal. While this highlights the role Mn–O covalency may play in Na-removal, we believe the water trafficking (co-deintercalation with Na-ion) at high potentials remains the primary factor in the observed shrinkage of the interlayer for $\text{Na}_{0.27}\text{MnO}_2$ for the following reasons. Firstly, compared to the LIB electrodes with an interlayer spacing < 3 Å, the $\text{Na}_{0.27}\text{MnO}_2$ system has an interlayer spacing of 7.1 Å. Thus, the oxygen-oxygen interaction between adjacent $[\text{MO}_6]$ layers in birnessite, which is inversely correlated to the square of the interlayer distance ($\propto \frac{1}{r^2}$ where *r* is the distance between neighboring

oxygen) is relatively weak compared to the NMC compounds. Moreover, the structural water within the interlayer of $\text{Na}_{0.27}\text{MnO}_2$ birnessite provides a “screening” effect that further weakens the O–O interaction, well described by Debye-Huckel theory.

Different from *c*-lattice collapse in charged LIB layered oxide, where the irreversible and large lattice collapse (up to 5%) results in the pulverization of electrode material and impairs their full utilization for Li-ion storage, the reversible co-deintercalation of structural water in $\text{Na}_{0.27}\text{MnO}_2$ benefits Na-ion storage. Notably, repetitive insertion and extraction of cations and thus drastic changes of the interlayer distance during prolonged cycling can cause the degradation of the electrode material. Figure 6 showed that as the *c*-lattice contracted, the *b*-lattice continue to decrease (d_{001} and d_{020} decreased). This indicates that the co-deintercalation of water molecules along with Na-ions stabilizes the layered structure against further expansion of the interlayer distance at higher voltages while sustaining an intensive redox process. To the best of our knowledge, this new safety mechanism has never been reported in aqueous energy storage. Notably, previous investigations of intercalation cations (e.g., Na^+ and Mg^{2+}) in aprotic electrolytes in layered materials have reported a similar water-assisted cation insertion, where insertion kinetics can be greatly improved since a water solvation shell partially shields the charge of cations within the cation/water co-intercalation compound^{59–63}.

Supplementary Figure 26 shows $\text{Na}_{0.19}\text{MnO}_2$ (synthesized via thermal decomposition of NaMnO_4 materials at 800 °C) had a lower amount of structural water compared with hydrated $\text{Na}_{0.27}\text{MnO}_2$ materials, evidenced by its narrower interlayer distance (0.713 nm vs 0.719 nm) as XRD showed (Supplementary Fig. 26). More importantly, the half-cell CP measurements showed that less hydrated $\text{Na}_{0.19}\text{MnO}_2$ birnessite had an inferior electrochemical performance to the hydrated $\text{Na}_{0.27}\text{MnO}_2$ in term of discharge capacity, rate performance and cycle life (Supplementary Fig. 27). For example, the hydrated $\text{Na}_{0.27}\text{MnO}_2$ showed a much higher discharge capacity (138 mAh g^{-1}) compared with less hydrated $\text{Na}_{0.19}\text{MnO}_2$ (60 mAh g^{-1}). Moreover, at a current density of 1 A g^{-1} , $\text{Na}_{0.27}\text{MnO}_2$ also demonstrated higher discharge capacities and higher capacity retention compared with $\text{Na}_{0.19}\text{MnO}_2$ throughout the first 100 charge and discharge cycles (53% vs 29% at 50th cycle and 35% vs 22% at 100th cycle), while maintaining comparable coulombic efficiencies. Thus, it is evident that structural water co-intercalation with Na-ions plays promotional roles in electrochemical performance.

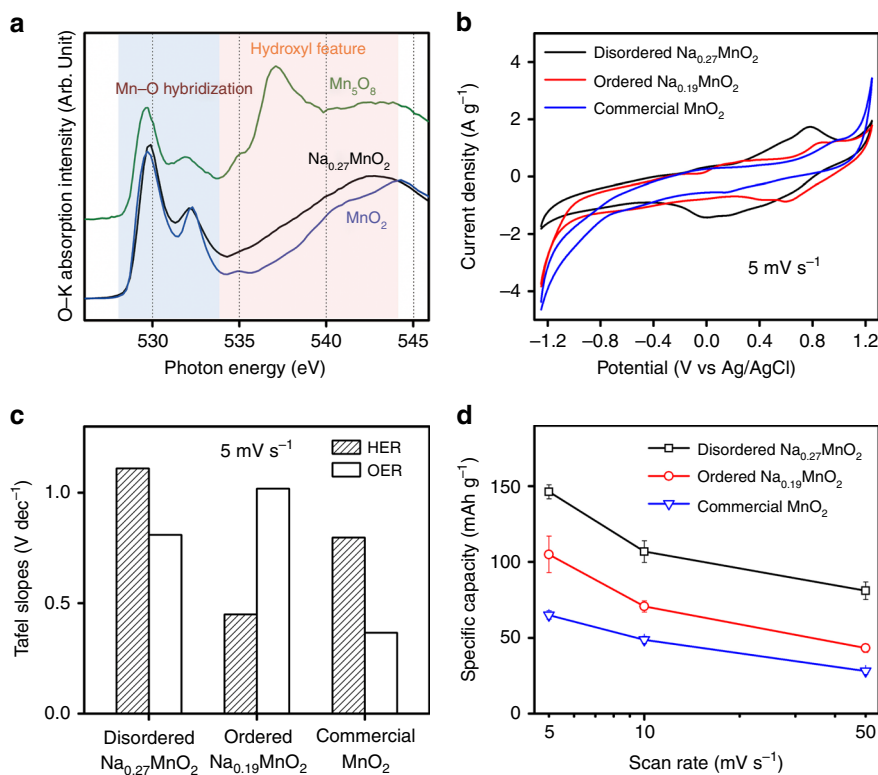


Fig. 8 The effects of disorder structure on the potential window. **a** Oxygen K-edge sXAS of electrochemically cycled $\text{Na}_{0.27}\text{MnO}_2$, Mn_5O_8 and commercial MnO_2 materials; **b** CV scans of disordered $\text{Na}_{0.27}\text{MnO}_2$, ordered $\text{Na}_{0.19}\text{MnO}_2$ and commercial MnO_2 materials at the scan rate of 5 mV s^{-1} in a 2.5 V potential window in half-cell; **c** calculated Tafel slopes of HER and OER at the scan rate of 5 mV s^{-1} ; **d** Specific capacities at the scan rate of 5, 10 and 50 mV s^{-1}

The disordered structure widens the voltage window. Although Mn_5O_8 and $\text{Na}_{0.27}\text{MnO}_2$ materials showed a 2.5 V stable voltage window for aqueous Na-ion storage (Supplementary Figs. 10, 28), the mechanisms underlying their high resistance toward HER and OER were completely different. Figure 8a shows that O-K sXAS spectra of $\text{Na}_{0.27}\text{MnO}_2$ and Mn_5O_8 have similar sharp features below 534 eV from the hybridization between the O 2p band and Mn 3d states. However, only the Mn_5O_8 material showed distinct fingerprint water-features at the 535 and 537 eV, indicating the formation of a highly ordered hydroxylated interphase on the surface as we reported previously⁴⁸. To understand role of disordered structure in mitigating the water decomposition, we synthesized ordered $\text{Na}_{0.19}\text{MnO}_2$ birnessite via thermal decomposition of NaMnO_4 materials at 800°C and conducted the Tafel analysis for hydrogen evolution reaction (HER) and oxygen evolution reaction (OER) on disordered $\text{Na}_{0.27}\text{MnO}_2$, ordered $\text{Na}_{0.19}\text{MnO}_2$ and commercial MnO_2 materials in a 0.1 M Na_2SO_4 electrolyte. XRD and X-ray PDF were conducted to compare the structural difference of three materials (Supplementary Fig. 29–30, Supplementary Tables 8–10), showing that disordered $\text{Na}_{0.27}\text{MnO}_2$ had a triclinic (C-1) birnessite structure. Though disordered $\text{Na}_{0.27}\text{MnO}_2$ and ordered $\text{Na}_{0.19}\text{MnO}_2$ both show the birnessite layered structure, $\text{Na}_{0.27}\text{MnO}_2$ has a smaller crystalline size and a shorter coherence length (Supplementary Fig. 29b) compared to $\text{Na}_{0.19}\text{MnO}_2$. On the other hand, commercial MnO_2 showed a highly crystalline and ordered $\beta\text{-MnO}_2$ phase. Supplementary Figure 30 demonstrated the difference of local structures between disordered $\text{Na}_{0.27}\text{MnO}_2$ and ordered $\text{Na}_{0.19}\text{MnO}_2$ birnessite and commercial MnO_2 , where the former showed a more disordered lattice structure.

Figure 8b shows the CVs of disordered $\text{Na}_{0.27}\text{MnO}_2$, ordered $\text{Na}_{0.19}\text{MnO}_2$ and commercial $\beta\text{-MnO}_2$ and a scan rate of 5 mV s^{-1}

(CVs tested at other scan rates are shown in Supplementary Fig. 31). Though all three materials were tested in a 2.5 V potential window, ordered $\text{Na}_{0.19}\text{MnO}_2$ and commercial $\beta\text{-MnO}_2$ materials displayed obvious gas evolution features at lower and higher potential ranges. The Tafel analysis showed that disordered $\text{Na}_{0.27}\text{MnO}_2$ displayed a much weaker HER current at potentials up to -1.25 V (overpotential of 0.63 V towards HER) and higher Tafel slopes at various scan rates (Fig. 8c, Supplementary Fig. 31), suggesting sluggish HER kinetics. It is notable that three materials were inactive towards OER even at a potential of 1.25 V (overpotential of 0.63 V towards OER), however, only disordered $\text{Na}_{0.27}\text{MnO}_2$ has high overpotential for both HER and OER, suggesting that the disordered nature leads to high resistance to the gas evolution reactions, thus a kinetically stable potential window of 2.5 V. Although ordered $\text{Na}_{0.19}\text{MnO}_2$ and commercial $\beta\text{-MnO}_2$ materials showed a great capacity enhancement at a lower potential range close to -1.25 V , probably benefiting from hydrogen insertion, disordered $\text{Na}_{0.27}\text{MnO}_2$ still showed much superior capacities at all tested scan rates. The inferior capacities from ordered $\text{Na}_{0.19}\text{MnO}_2$ and commercial $\beta\text{-MnO}_2$ might be due to the parasitic gas evolution reactions especially HER that degraded the electrode and causes capacity loss at prolonged cycles. Previous DFT calculations demonstrated that the thermodynamically unstable edge sites of the layered transition-metal dichalcogenides nanocrystals were catalytically active for HER⁴⁷. Previous studies showed that HER current was proportional to the length of edges rather than the coverage area of catalysts^{64,65}, but these catalytically active sites were located on the thermodynamically unstable planes (edges of the layers), which are difficult to be exposed preferentially^{66,67}. In this study, disordered MnO_2 layered structures have highly exposed (001) planes that are thermodynamically stable plane but

catalytically inert, while the ordered $\text{Na}_{0.19}\text{MnO}_2$ birnessite possesses a large grain size with a long coherent length, therefore the edges of the layers that are more active toward gas evolution are likely exposed.

Discussion

In this work, we have integrated detailed structural analysis with electrochemical measurements to understand the observed high capacity and good structural stability found in the disordered and Na-rich $\text{Na}_{0.27}\text{MnO}_2$ birnessite layered materials. In situ XRD has revealed the role of water co-deintercalation in mitigating inter-layer expansion during the high potential charging. Investigations of solvent co-intercalation properties in other layered materials will be useful in designing high capacity rechargeable aqueous batteries. In addition to water trafficking, our results also manifest the promotional effects of the disordered structure on aqueous Na-ion storage: disordered $\text{Na}_{0.27}\text{MnO}_2$ structure allows continuous and smooth structural evolution during the charging and discharging processes without phase transitions and possesses highly exposed (001) planes with low density of active edge sites for gas evolution reactions, and thus yields a large aqueous Na-ion storage capacity and long cycling life. The reported results have provided the insight underlying the promotional roles of structural water and disordered electrode structure for aqueous Na-ion storage. Especially, the structural water trafficking at high potential charging discovered here may provide a fundamental leap forward in current understanding how water molecules stabilize the electrode structure during redox processes.

Methods

Material synthesis. Mn_3O_4 nanoparticles were first synthesized via a solution phase method. In a typical synthesis, $\text{MnCl}_2 \cdot 4\text{H}_2\text{O}$ (0.7 g, Alfa Aesar, 99% metals basis) was fully dissolved by deionized water (140 mL, 18.2 M Ω ; Millipore, Inc.) in a 500 mL flask under vigorous stirring at room temperature. The aqueous solution of NaOH (Alfa Aesar, 99.98% metals basis) with a concentration of 0.123 g mL⁻¹ was injected at a rate of 0.167 mL min⁻¹ for 50 min using an automatic syringe (HSW Inc.). After injection, the mixture continuously reacted for another 30 min till dark brown precipitate was formed. The resulting product was separated by centrifuging and then washed by deionized water and ethanol consecutively. The obtained products (Mn_3O_4 nanoparticles) were finally vacuum-dried. In the synthesis of sodium-manganese oxides, NaOH (Alfa Aesar, 99.99% metals basis) and 100 mg Mn_3O_4 nanoparticles were grounded using a mortar and pestle with the molar ratios of 0.5, 1, 1.5, 2, and 4, respectively. The resulting mixture of NaOH and Mn_3O_4 was heated in a tube furnace (Thermal Scientific, Inc.) in open air at 270 °C for 6 h. The obtained solids were thoroughly washed with deionized water to remove the possible NaOH residual and vacuum-dried for overnight. Ordered $\text{Na}_{0.19}\text{MnO}_2$ birnessite was synthesized via thermal decomposition of NaMnO_4 at 800 °C for 12 h, and then washed by deionized water and ethanol, and dried in vacuum. The MnO_2 birnessite with low sodium concentration $\text{Na}_{0.13}\text{MnO}_2$ was synthesized via a wet chemistry method. Aqueous MnCl_2 (5 mg mL⁻¹) precursor was injected into 20 mL NaOH solution with a concentration of 5.7 mg mL⁻¹ at the rate of 0.167 mL min⁻¹ for 1 h, and the obtained product was vacuum-dried after washed by deionized water and ethanol. And then the solids were annealed in air at 270 °C for 6 h.

Material characterizations. Inductively coupled plasma mass spectrometry (ICP-MS) was used to identify the elemental ratios of materials. Sample aliquots were digested in mixed concentrated HCl-HNO₃ solution and then transferred into HNO₃ solution for dilution in 2% HNO₃ and introduction into the Nu instruments AttoM high resolution ICP-MS. Standards of known concentrations were used to correct for drift and within-instrument elemental fractionation. Triplicate runs of each sample allowed for the determination of the precision of each sample. Energy dispersive X-ray spectroscopy (EDXS) was conducted for elemental analysis by an Amray 3300FE field emission SEM with a PGT Imix-PC microanalysis system at the University of New Hampshire. Thermogravimetric analysis (TGA) was measured on a Mettler-Toledo instrument at the University of New Hampshire. Regular transmission electron microscopy (TEM) images were collected on Zeiss/LEO 922 Omega TEM at the University of New Hampshire. X-ray photoelectron spectroscopy (XPS) was measured using Thermo Scientific K-Alpha instrument at Harvard University.

Half-cell test. Cyclic voltammetry (CV) measurements of sodium-manganese oxide were conducted using a three-electrode half-cell powered by CHI 660d single

channel electrochemical workstation. The three-electrode system contained a glassy carbon rotating disc electrode (Pine Instrument) as the working electrode, platinum wire and silver-silver chloride (Ag/AgCl) electrode as counter and reference electrodes, respectively. The ink material was prepared by grinding mixture of 7 mg sodium-manganese oxide and 3 mg carbon black (Alfa Aesar, > 99.9%). The resulting mixture was mixed with deionized water to make an ink solution of 0.5 mg mL⁻¹. The resulting solution was subsequently sonicated until the materials were homogeneously dispersed. In a typical half-cell measurement, 10 μL suspension containing 3.5 μg sodium-manganese oxide and 1.5 μg carbon black was drop-cast onto the glassy carbon disc electrode (0.5 cm in diameter) and vacuum-dried. The CV measurements of electrodes were conducted in a 250 mL flat-bottom flask containing 100 mL argon-purged Na_2SO_4 aqueous electrolyte (0.1 M) at a rotating rate of 500 rpm. The CV data were obtained within an applied potential range from -1.25 V to 1.25 V (vs Ag/AgCl) for three cycles, and the third CV cycle was used for the calculation of storage capacity. The CP measurements of $\text{Na}_{0.27}\text{MnO}_2$ in a three-electrode half-cell was also conducted at the current densities from 0.3 A g⁻¹ to 2.0 A g⁻¹ with potential from -0.75 V to 1.25 V (vs Ag/AgCl). $\text{Na}_{0.27}\text{MnO}_2$ was charged to 1.25 V (vs Ag/AgCl) from open circuit voltage in 0.5 M Na_2SO_4 solution with a scan rate of 1 mV s⁻¹ by using CV in half-cell, and then discharged to -1.25 V. The charged and discharged samples were washed and collected for ex-situ XPS measurements.

Diffusivity measurements. The diffusivity measurements were tested in a typical half-cell setting as described above, except 40 μg active materials sodium-manganese oxides was loaded on working electrode and 0.25 M Na_2SO_4 was used as the electrolyte. A constant negative current pulse of 1 μA was first applied to the working electrode and was held for 15 s to discharge the electrode from the open circuit potential. After that, the working electrode was relaxed and potential changes were collected for another 1000 s.

Potential of zero charge. The potential of zero charge (pzc) of $\text{Na}_{0.27}\text{MnO}_2$ materials was estimated using an open circuit voltage (OCV) measurement using a three-electrode cell in a 0.1 M Na_2SO_4 electrolyte. Supplementary Figure 32 shows that the initial potential of the electrode was 0.47 V (vs Ag/AgCl), slowly increased to a rather stable value of 0.50 V after 2 h without an external field. In this context, pzc of $\text{Na}_{0.27}\text{MnO}_2$ materials should be around 0.5 V vs. Ag/AgCl. As a higher (or lower) external potential is applied, the materials will be oxidized (or reduced) by Na-ion extraction (or insertion).

Full-cell test. Symmetric two-electrode full-cells with $\text{Na}_{0.27}\text{MnO}_2$ electrodes were assembled and measured to characterize the energy/power performance and the long cycle stability as well. Electrodes were made by drop casting the slurry containing ~5 mg $\text{Na}_{0.27}\text{MnO}_2$ and 1.25 mg carbon black as a mass ratio of 4:1 on Toray carbon paper (E-Tek, Inc., 1.5 cm in diameter). The resulting electrodes were weighed with an accurate mass loading of active material after vacuum-dried overnight. Two symmetric electrodes were separated by cellulose-based filter paper (Whatman), and 150 μL Na_2SO_4 aqueous solution (1 M) was used as the electrolyte. The cell stack of electrodes and separator were tightened by stainless plate and compression spring to ensure good electrical contact and then assembled in the split button-cells (model: EQ-STC, MTI Corp.). Galvanostatic charge and discharge measurements of symmetric full-cells were conducted on the battery analyzer (model: B-TG, Arbin Instruments) within 2.5 V potential window for 5000 cycles at the constant current densities of 1, 2, 5, and 10 A g⁻¹. All the electrochemical calculations are provided in the supporting information. Toray paper was used as current collector for symmetric full-cell measurements and stable in 2.5 V without obvious generation of hydrogen (Supplementary Fig. 17).

Electrochemical impedance measurements. Electrochemical impedance spectroscopy (EIS) measurements were conducted after each charge and discharge cycle in full cell at the open circuit potential with a perturbation of 5 mV and frequency range from 0.1 to 100 kHz, and the Nyquist plots were collected.

X-ray and neutron scattering characterizations. X-ray diffraction measurements were conducted at Beamline 17-BM-B at the Advanced Photon Source at the Argonne National Laboratory with a wavelength of $\lambda = 0.72768 \text{ \AA}$. In situ XRD of electrochemical half-cell measurements were conducted in a home-made cell consisted of thin carbon paper (E-Tek, Inc.) as working electrode, platinum wire and micro Ag/AgCl electrode as counter and reference electrodes, respectively. The Na_2SO_4 aqueous electrolyte (1 M) was used as the electrolyte. The suspension of a mixture of $\text{Na}_{0.27}\text{MnO}_2$ and carbon black was drop-cast on the thin carbon paper and then dried naturally in air. The cellulose-based filter paper was used as a separator. The cell was then assembled for X-ray measurements. In situ XRD tests were performed during CV scans from -1.25 V to 1.25 V (vs Ag/AgCl) at the scan rates of 0.75 mV s⁻¹. GSAS-II software was used to analyze the structural changes during the charge and discharge processes. The X-ray total scattering experiment was also conducted at Beamline 17-BM-B using a wavelength of 0.24116 \AA . The total neutron scattering experiment was conducted at the Nanoscale-Ordered Materials Diffractometer (NOMAD) beamline at Spallation Neutron Source at Oak

Ridge National Laboratory. The atomic Pair Distribution Function (PDF) analysis was conducted using PDFgui software.

Theoretical methods. Density functional theory (DFT) calculations were performed using the WIEN2k software package, which uses full potential and linearized augmented plane waves with local orbitals (LAPW + lo) to self-consistently solve the Kohn-Sham equations⁶¹. The generalized gradient approximation of Perdew, Burke, and Ernzerhof (GGA-PBE) was used for the exchange and correlation energies⁶². The plane-wave cutoff parameters $R_{MT}K_{max}$ and G_{max} were selected as 6.5 and 12, respectively, and the cutoff energy was -6.0 Ry. The k-points of the cell was $(1 \times 12 \times 4)$ and for the $\text{NaMnO}_2 \cdot \text{H}_2\text{O}$.

Data availability

The authors declare that the data supporting the findings of this study are available within the paper and its supplementary information files.

Received: 12 February 2018; Accepted: 12 October 2019;

Published online: 31 October 2019

References

- Yabuuchi, N. et al. P2-type $\text{Na}_x[\text{Fe}_{1/2}\text{Mn}_{1/2}\text{O}]_2$ made from earth-abundant elements for rechargeable Na batteries. *Nat. Mater.* **11**, 512–517 (2012).
- Kim, H. et al. Aqueous rechargeable Li and Na ion batteries. *Chem. Rev.* **114**, 11788–11827 (2014).
- Wessells, C. D., Huggins, R. A. & Cui, Y. Copper hexacyanoferrate battery electrodes with long cycle life and high power. *Nat. Commun.* **2**, 5 (2011).
- Pasta, M., Wessells, C. D., Huggins, R. A. & Cui, Y. A high-rate and long cycle life aqueous electrolyte battery for grid-scale energy storage. *Nat. Commun.* **3**, 7 (2012).
- Pasta, M. et al. Manganese-cobalt hexacyanoferrate cathodes for sodium-ion batteries. *J. Mater. Chem. A* **4**, 4211–4223 (2016).
- Wang, L. et al. A superior low-cost cathode for a Na-ion battery. *Angew. Chem. Int. Ed.* **52**, 1964–1967 (2013).
- Song, J. et al. Removal of interstitial H_2O in hexacyanometallates for a superior cathode of a sodium-ion battery. *J. Am. Chem. Soc.* **137**, 2658–2664 (2015).
- Lu, Y. H., Wang, L., Cheng, J. G. & Goodenough, J. B. Prussian blue: a new framework of electrode materials for sodium batteries. *Chem. Commun.* **48**, 6544–6546 (2012).
- Caballero, A. et al. Synthesis and characterization of high-temperature hexagonal P2- $\text{Na}_{0.6}\text{MnO}_2$ and its electrochemical behaviour as cathode in sodium cells. *J. Mater. Chem.* **12**, 1142–1147 (2002).
- Clement, R. J., Bruce, P. G. & Grey, C. P. Review- Manganese-based P2-type transition metal oxides as sodium-ion battery cathode materials. *J. Electrochem. Soc.* **162**, A2589–A2604 (2015).
- Kubota, K., Yabuuchi, N., Yoshida, H., Dahbi, M. & Komaba, S. Layered oxides as positive electrode materials for Na-ion batteries. *MRS Bull.* **39**, 416–422 (2014).
- Delmas, C., Fouassier, C. & Hagenmuller, P. Structural classification and properties of the layered oxides. *Phys. B C.* **99**, 81–85 (1980).
- Mendiboure, A., Delmas, C. & Hagenmuller, P. Electrochemical intercalation and deintercalation of Na_xMnO_2 bronzes. *J. Solid State Chem.* **57**, 323–331 (1985).
- Doeff, M. M., Peng, M. Y., Ma, Y. P. & Dejonghe, L. C. Orthorhombic Na_xMnO_2 as a cathode material for secondary sodium and lithium polymer batteries. *J. Electrochem. Soc.* **141**, L145–L147 (1994).
- Kim, S., Ma, X. H., Ong, S. P. & Ceder, G. A comparison of destabilization mechanisms of the layered Na_xMO_2 and Li_xMO_2 compounds upon alkali deintercalation. *Phys. Chem. Chem. Phys.* **14**, 15571–15578 (2012).
- Li, X. et al. Jahn-teller assisted Na diffusion for high performance Na ion batteries. *Chem. Mat.* **28**, 6575–6583 (2016).
- Tian, M., Gao, Y. R., Wang, Z. X. & Chen, L. Q. Understanding structural stability of monoclinic LiMnO_2 and NaMnO_2 upon de-intercalation. *Phys. Chem. Chem. Phys.* **18**, 17345–17350 (2016).
- Choi, Y. & Liu, P. Understanding of ethanol decomposition on Rh(111) from density functional theory and kinetic Monte Carlo simulations. *Catal. Today* **165**, 64–70 (2011).
- Kubota, K., Kumakura, S., Yoda, Y., Kuroki, K. & Komaba, S. Electrochemistry and solid-state chemistry of NaMeO_2 (Me=3d transition metals). *Adv. Energy Mater.* **8**, 40 (2018).
- Lee, D. H., Xu, J. & Meng, Y. S. An advanced cathode for Na-ion batteries with high rate and excellent structural stability. *Phys. Chem. Chem. Phys.* **15**, 3304–3312 (2013).
- Yeager, M. et al. Highly efficient $\text{K}_{0.15}\text{MnO}_2$ birnessite nanosheets for stable pseudocapacitive cathodes. *J. Phys. Chem. C.* **116**, 20173–20181 (2012).
- Qu, Q. et al. Electrochemical performance of MnO_2 nanorods in neutral aqueous electrolytes as a cathode for asymmetric supercapacitors. *J. Phys. Chem. C.* **113**, 14020–14027 (2009).
- Wang, J., Zhang, G. & Zhang, P. Layered birnessite-type MnO_2 with surface pits for enhanced catalytic formaldehyde oxidation activity. *J. Mater. Chem. A* **5**, 5719–5725 (2017).
- Zhu, H. T. et al. Birnessite-type MnO_2 nanowalls and their magnetic properties. *J. Phys. Chem. C.* **112**, 17089–17094 (2008).
- Cai, J., Liu, J. & Suib, S. L. Preparative parameters and framework dopant effects in the synthesis of layer-structure birnessite by air oxidation. *Chem. Mater.* **14**, 2071–2077 (2002).
- Brousse, T., Toupin, M. & Belanger, D. A hybrid activated carbon-manganese dioxide capacitor using a mild aqueous electrolyte. *J. Electrochem. Soc.* **151**, A614–A622 (2004).
- Athouel, L. et al. Variation of the MnO_2 birnessite structure upon charge/discharge in an electrochemical supercapacitor electrode in aqueous Na_2SO_4 electrolyte. *J. Phys. Chem. C.* **112**, 7270–7277 (2008).
- Liu, Y. et al. High-performance aqueous sodium-ion batteries with $\text{K}_{0.27}\text{MnO}_2$ cathode and their sodium storage mechanism. *Nano Energy* **5**, 97–104 (2014).
- Suo, L. M. et al. “Water-in-salt” electrolyte enables high-voltage aqueous lithium-ion chemistries. *Science* **350**, 938–943 (2015).
- Xu, K. & Wang, C. S. Widening voltage windows. *Nat. Energy* **1**, 16161 (2016).
- Yamada, Y. et al. Hydrate-melt electrolytes for high-energy-density aqueous batteries. *Nat. Energy* **1**, 16129 (2016).
- Peng, L. et al. Ultrathin two-dimensional MnO_2 /graphene hybrid nanostructures for high-performance, flexible planar supercapacitors. *Nano Lett.* **13**, 2151–2157 (2013).
- Yeager, M. P. et al. Pseudocapacitive hausmannite nanoparticles with (101) facets: synthesis, characterization, and charge-transfer mechanism. *ChemSusChem* **6**, 1983–1992 (2013).
- Chen, R., Zavalij, P. & Whittingham, M. S. Hydrothermal synthesis and characterization of $\text{K}_x\text{MnO}_2 \cdot y\text{H}_2\text{O}$. *Chem. Mater.* **8**, 1275–1280 (1996).
- Park, Y. J. & Doeff, M. A. Synthesis and electrochemical characterization of $\text{M}_2\text{Mn}_2\text{O}_8$ (M=Ca, Cu) compounds and derivatives. *Solid State Ion.* **177**, 893–900 (2006).
- Pan, H. et al. Reversible aqueous zinc/manganese oxide energy storage from conversion reactions. *Nat. Energy* **1**, 16039 (2016).
- Sun, W. et al. Zn/ MnO_2 battery chemistry with H^+ and Zn^{2+} coinsertion. *J. Am. Chem. Soc.* **139**, 9775–9778 (2017).
- Huang, J. et al. Polyaniline-intercalated manganese dioxide nanolayers as a high-performance cathode material for an aqueous zinc-ion battery. *Nat. Commun.* **9**, 2906 (2018).
- Li, Z., Young, D., Xiang, K., Carter, W. C. & Chiang, Y.-M. Towards high power high energy aqueous sodium-ion batteries: the $\text{NaTi}_2(\text{PO}_4)_3/\text{Na}_{0.44}\text{MnO}_2$ system. *Adv. Energy Mater.* **3**, 290–294 (2013).
- Lee, J. et al. Reversible $\text{Mn}^{2+}/\text{Mn}^{4+}$ double redox in lithium-excess cathode materials. *Nature* **556**, 185–190 (2018).
- Liu, T. C., Pell, W. G., Conway, B. E. & Roberson, S. L. Behavior of molybdenum nitrides as materials for electrochemical capacitors: comparison with ruthenium oxide. *J. Electrochem. Soc.* **145**, 1882–1888 (1998).
- Nagasubramanian, G., Jungst, R. G. & Doughty, D. H. Impedance, power, energy, and pulse performance characteristics of small commercial Li-ion cells. *J. Power Sources* **83**, 193–203 (1999).
- Wu, Z.-S. et al. High-energy MnO_2 nanowire/graphene and graphene asymmetric electrochemical capacitors. *ACS Nano* **4**, 5835–5842 (2010).
- He, Y. et al. Freestanding three-dimensional graphene/ MnO_2 composite networks as ultralight and flexible supercapacitor electrodes. *ACS Nano* **7**, 174–182 (2013).
- Zhang, D., Zhang, Y., Luo, Y. & Chu, P. K. Highly porous honeycomb manganese oxide@carbon fibers core-shell nanocables for flexible supercapacitors. *Nano Energy* **13**, 47–57 (2015).
- Hou, Z., Li, X., Liang, J., Zhu, Y. & Qian, Y. An aqueous rechargeable sodium ion battery based on a NaMnO_2 - $\text{NaTi}_2(\text{PO}_4)_3$ hybrid system for stationary energy storage. *J. Mater. Chem. A* **3**, 1400–1404 (2015).
- Brousse, T. et al. Long-term cycling behavior of asymmetric activated carbon/ MnO_2 aqueous electrochemical supercapacitor. *J. Power Sources* **173**, 633–641 (2007).
- Shan, X. Q. et al. Bivalence Mn_5O_8 with hydroxylated interphase for high-voltage aqueous sodium-ion storage. *Nat. Commun.* **7**, 8 (2016).
- Yu, X. & Manthiram, A. Performance enhancement and mechanistic studies of room-temperature sodium-sulfur batteries with a carbon-coated functional nafion separator and a Na_2S /activated carbon nanofiber cathode. *Chem. Mater.* **28**, 896–905 (2016).
- Zheng, J., Yan, P., Kan, W. H., Wang, C. & Manthiram, A. A spinel-integrated P2-type layered composite: high-rate cathode for sodium-ion batteries. *J. Electrochem. Soc.* **163**, A584–A591 (2016).

51. Kang, B. & Ceder, G. Battery materials for ultrafast charging and discharging. *Nature* **458**, 190–193 (2009).
52. Charles, D. S. et al. Structural water engaged disordered vanadium oxide nanosheets for high capacity aqueous potassium-ion storage. *Nat. Commun.* **8**, 15520 (2017).
53. Liu, J. et al. Large-scale synthesis and comprehensive structure study of delta-MnO₂. *Inorg. Chem.* **57**, 6873–6882 (2018).
54. Radin, M. D. et al. Narrowing the gap between theoretical and practical capacities in Li-ion layered oxide cathode materials. *Adv. Energy Mater.* **7**, 1602888 (2017).
55. Li, W., Asl, H. Y., Xie, Q. & Manthiram, A. Collapse of LiNi_{1-x-y}Co_xMn_yO₂ lattice at deep charge irrespective of nickel content in lithium-ion batteries. *J. Am. Chem. Soc.* **141**, 5097–5101 (2019).
56. Kondrakov, A. O. et al. Charge-transfer-induced lattice collapse in Ni-Rich NCM cathode materials during delithiation. *J. Phys. Chem. C* **121**, 24381–24388 (2017).
57. Grenier, A. et al. Reaction heterogeneity in LiNi_{0.8}Co_{0.15}Al_{0.05}O₂ induced by surface layer. *Chem. Mater.* **29**, 7345–7352 (2017).
58. Scofield J. H. Theoretical photoionization cross sections from 1 to 1500 keV. (Lawrence Livermore Laboratory, U.S. Atomic Energy Commission, 1973).
59. Spahr, M. E., Novák, P., Haas, O. & Nesper, R. Electrochemical insertion of lithium, sodium, and magnesium in molybdenum(VI) oxide. *J. Power Sources* **54**, 346–351 (1995).
60. Levi, E., Gofer, Y. & Aurbach, D. On the way to rechargeable Mg batteries: the challenge of new cathode materials. *Chem. Mater.* **22**, 860–868 (2010).
61. Sai Gautam, G., Canepa, P., Richards, W. D., Malik, R. & Ceder, G. Role of structural H₂O in intercalation electrodes: the case of Mg in nanocrystalline Xerogel-V₂O₅. *Nano Lett.* **16**, 2426–2431 (2016).
62. Lim, S. Y. et al. Lattice water for the enhanced performance of amorphous iron phosphate in sodium-ion batteries. *ACS Energy Lett.* **2**, 998–1004 (2017).
63. Nam, K. W. et al. Critical role of crystal water for a layered cathode material in sodium ion batteries. *Chem. Mater.* **27**, 3721–3725 (2015).
64. Hinnemann, B. et al. Biomimetic hydrogen evolution: MoS₂ Nanoparticles as catalyst for hydrogen evolution. *J. Am. Chem. Soc.* **127**, 5308–5309 (2005).
65. Jaramillo, T. F. et al. Identification of active edge sites for electrochemical H₂ evolution from MoS₂ nanocatalysts. *Science* **317**, 100–102 (2007).
66. Kong, D. et al. Synthesis of MoS₂ and MoSe₂ films with vertically aligned layers. *Nano Lett.* **13**, 1341–1347 (2013).
67. Kibsgaard, J., Chen, Z., Reinecke, B. N. & Jaramillo, T. F. Engineering the surface structure of MoS₂ to preferentially expose active edge sites for electrocatalysis. *Nat. Mater.* **11**, 963 (2012).

Acknowledgements

This work was supported by the US Department of Energy (DOE), Office of Science, Basic Energy Sciences under Award # DE-SC0010286 (X.T., X.S., F.G., D.C.). The research at Binghamton University is partially supported by NSF DMREF-1627583. This research used Beamline 17-BM-B of the Advanced Photon Source, a U.S. Department of Energy (DOE) Office of Science User Facility operated for the DOE Office of Science by Argonne National Laboratory under Contract No. DE-AC02-06CH11357. The Advanced

Light Source is supported by the Director, Office of Science, Office of Basic Energy Sciences, of the U.S. Department of Energy under Contract No. DE-AC02-05CH11231. The neutron scattering experiments were carried out at the Spallation Neutron Source, which is sponsored by the Scientific User Facilities Division, Office of Basic Energy Sciences, US Department of Energy, under Contract No. DE-AC05-00OR22725 with Oak Ridge National Laboratory.

Author contributions

All authors contributed to the preparation of the manuscript. X.S. contributed to the material synthesis and characterizations, electrochemical experimental measurements and analysis, X-ray analysis. F.G., X.S., and D.S.C. contributed to neutron PDF analysis. X.S. and W.X. contributed to X-ray measurement. Z.L.H., S.A.R., and L.F.J.P. contributed to XPS and DFT calculations. J.W. and W.Y. contributed to sXAS measurement and analysis. K.P., J.N., and M.F. contributed to the neutron measurements. X.S. and X.T. wrote the manuscript. X.T. contributed to the design of the experiments.

Competing interests

The authors declare no competing interests.

Additional information

Supplementary information is available for this paper at <https://doi.org/10.1038/s41467-019-12939-3>.

Correspondence and requests for materials should be addressed to X.T.

Peer review information *Nature Communications* thanks Jacob Olchowka and the other, anonymous, reviewer(s) for their contribution to the peer review of this work.

Reprints and permission information is available at <http://www.nature.com/reprints>

Publisher's note Springer Nature remains neutral with regard to jurisdictional claims in published maps and institutional affiliations.



Open Access This article is licensed under a Creative Commons Attribution 4.0 International License, which permits use, sharing, adaptation, distribution and reproduction in any medium or format, as long as you give appropriate credit to the original author(s) and the source, provide a link to the Creative Commons license, and indicate if changes were made. The images or other third party material in this article are included in the article's Creative Commons license, unless indicated otherwise in a credit line to the material. If material is not included in the article's Creative Commons license and your intended use is not permitted by statutory regulation or exceeds the permitted use, you will need to obtain permission directly from the copyright holder. To view a copy of this license, visit <http://creativecommons.org/licenses/by/4.0/>.

© The Author(s) 2019